



# Near-infrared to visible photon transition by upconverting $\text{NaYF}_4$ : $\text{Yb}^{3+}$ , $\text{Gd}^{3+}$ , $\text{Tm}^{3+}$ @ $\text{Bi}_2\text{WO}_6$ core@shell composite for bisphenol A degradation in solar light



Hassan Anwer, Jae-Woo Park\*

Department of Civil and Environmental Engineering, Hanyang University, 222-Wangsimni-ro, Seoul, 04763, South Korea

## ARTICLE INFO

**Keywords:**  
Upconverting nanoparticles  
 $\text{Bi}_2\text{WO}_6$   
Core@shell  
Solar radiation  
Bisphenol A

## ABSTRACT

The effective use of sunlight by photocatalyst systems is challenging. Here, we report an active-core@inert-shell nanohybrid composite that converts incompatible near-infrared (NIR) radiation to functional ultraviolet-visible (UV-vis) photons. The active core is composed of  $\text{NaYF}_4$ :  $\text{Yb}^{3+}$ ,  $\text{Gd}^{3+}$ , and  $\text{Tm}^{3+}$  upconverting nanoparticles (UCNPs). An inert bismuth tungstate ( $\text{Bi}_2\text{WO}_6$ ) shell with a narrow band gap (2.65 eV) was grown over the core via ethylenediaminetetraacetic acid-metal complex formation. Solar infrared photons were successfully converted to UV-vis photons, which activated the  $\text{Bi}_2\text{WO}_6$  shell via Förster resonance energy transfer (FRET). The high UV-vis-NIR response of the UCNP@ $\text{Bi}_2\text{WO}_6$  composite was demonstrated by 94% degradation of Bisphenol A in 180 min. Integrating UCNPs with  $\text{Bi}_2\text{WO}_6$  resulted in a high quantum yield of  $3.16 \times 10^{-5}$  molecules/photon, which is superior to the yield of the photocatalysts currently used. High photocurrent density (0.78 mA/cm<sup>2</sup>) confirmed the excellent photoelectrochemical potential for water splitting. Hydroxyl radicals generated at the valence band and superoxide radicals at defect sites in the  $\text{Bi}_2\text{WO}_6$  explain the excellent catalytic activity of UCNP@ $\text{Bi}_2\text{WO}_6$ . A figure of merit (FOM) reflecting important operational parameters was calculated and compared with previous reports for catalytic performance evaluation. The high FOM value of the UCNP@ $\text{Bi}_2\text{WO}_6$  hybrid composite indicates its excellent potential for practical applications.

## 1. Introduction

Photocatalysis has evolved into a green technology with applications in many emerging fields [1]. The most well-known photocatalyst semiconductor materials, such as  $\text{TiO}_2$ ,  $\text{ZnO}$ ,  $\text{ZrO}_2$ ,  $\text{ZnS}$ , and  $\text{SnO}_2$ , operate under ultraviolet (UV) radiation [2]. Visible light, which constitutes about 45% of the solar spectrum, can be used by narrow band-gap semiconductors, such as  $\text{CdS}$ ,  $\text{CdSe}$ ,  $\text{Fe}_2\text{O}_3$ ,  $\text{Ag}_3\text{PO}_4$ , and  $\text{C}_3\text{N}_4$ , to generate electron-hole pairs for redox reactions [3–5]. While much attention has been focused on UV-visible (UV-vis) active hybrid photocatalysts, infrared radiation, which forms 50% of the solar spectrum, has been relatively overlooked. This substantial waste of energy is of concern and photocatalysts that can use a maximal part of the solar spectrum are clearly needed [6]. Integrating photon upconverting nanoparticles (UCNPs) with a narrow band-gap photocatalyst can potentially yield a solution to the low photon utilization of conventional materials [7]. The upconverted photons emitted in the UV-vis spectrum can be used by a photocatalyst for its activation. Composites of UCNPs and different photocatalysts, such as  $\text{ZnO}$ ,  $\text{TiO}_2$  and  $\text{TiO}_2/\text{Au}$ , have been

reported [8–11]. Due to the large band gaps, those composites use only UV photons via near infrared (NIR) upconversion. Heterojunction metal sulfides with small band gaps solved the light absorption problem. However, photocorrosion of sulfide photocatalysts and their consequent leaching is still a dilemma [12,13]. Previously reported UCNPs also suffer from distortion in the lattice configuration after photocatalyst incorporation [14]. UCNPs in combination with conventional photocatalysts such as  $\text{CdS}$  and  $\text{ZnO}$  have also been investigated [15,16]. Those catalysts were limited by their low quantum yields, due to either unsuitable band edge position or ineffective energy transfer from the core to the shell. Therefore, combinations of UCNPs and photocatalysts need to be improved by enhancing UV-vis light absorption, lowering the band gap, and ensuring excellent core@shell morphology for effective energy transfer between core and shell.

UCNPs are generally composed of three integral parts: a host matrix, sensitizer, and activator [17]. The hexagonal  $\text{NaYF}_4$  host matrix is known for its excellent stability and NIR photon migration in the lattice [18,19]. Its low phonon energy also suppresses non-radiative relaxation and energy loss. Integrating a  $\text{NaYF}_4$  host lattice with a sensitizer that

\* Corresponding author.

E-mail address: [jaewoopark@hanyang.ac.kr](mailto:jaewoopark@hanyang.ac.kr) (J.-W. Park).

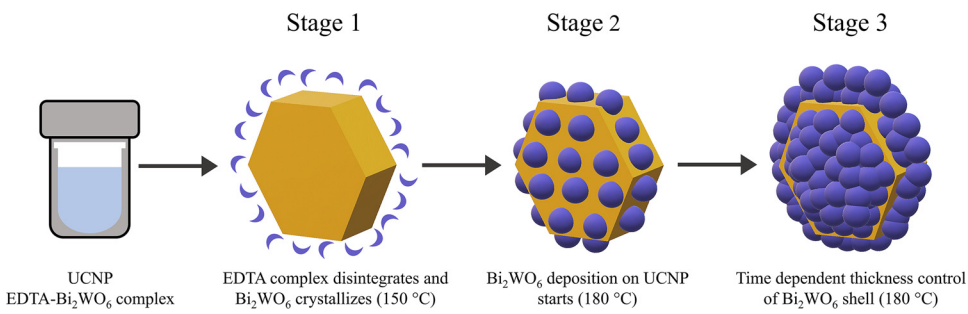


Fig. 1. Schematic of the formation and growth of the Bi<sub>2</sub>WO<sub>6</sub> shell on the UCNP core.

has a large absorption cross section could form an ideal UCNP core. Trivalent ytterbium (Yb<sup>3+</sup>) with a relatively large absorption cross-section of  $9.11 \times 10^{-21}$  cm<sup>2</sup> and a single excited energy level (<sup>2</sup>F<sub>5/2</sub>) makes an excellent sensitizer [20,21]. Upconversion also relies on the type of activator ions in the UCNP lattice. Energy transfer upconversion (ETU) is considered to be the most efficient of the five basic mechanisms for energy transfer and photon upconversion by UCNPs, as shown in Fig. S1. Trivalent thulium ions (Tm<sup>3+</sup>), which have adequate intermediate energy states and a ladder-like configuration of energy levels, are appropriate for ETU [22]. The upconversion can be further improved in the UV range by doping with gadolinium ions (Gd<sup>3+</sup>) [23]. Lanthanides are well known for their photon upconversion properties. In this research, we embedded NaYF<sub>4</sub>, the host matrix, with a lanthanide sensitizer (Yb<sup>3+</sup>) and activators (Tm<sup>3+</sup> and Gd<sup>3+</sup>) to upconvert NIR to UV-vis light.

Bismuth tungstate (Bi<sub>2</sub>WO<sub>6</sub>), a visible-light-active photocatalyst, has been used to effectively degrade organic contaminants into simpler forms [24–26]. Its physical and chemical stability, as well as its excellent catalytic activity, piezo- and pyro-electricity, and non-linear dielectric sensitivity, make it an important photocatalyst [27]. The drawback of electron-hole recombination can be overcome by doping Bi<sub>2</sub>WO<sub>6</sub> with a rare earth metal, which efficiently suppresses the charge recombination rate [28]. Herein, we report a nanocomposite of a Bi<sub>2</sub>WO<sub>6</sub> shell with a UCNP core that can harvest visible light and NIR photons for photocatalytic applications. Most wet chemistry methods to fabricate core@shell structures involve reduction, precipitation, and deposition, which require either acidic or basic pH [29]. UCNP cores are sensitive to extreme pH conditions, and therefore, in this research, we assembled the Bi<sub>2</sub>WO<sub>6</sub> shell around the core using a unique synthesis approach at a neutral/slightly basic pH. Because Bi<sub>2</sub>WO<sub>6</sub> is insoluble in water at neutral pH, we synthesized an ethylenediaminetetraacetic acid (EDTA)-metal complex and achieved Bi<sub>2</sub>WO<sub>6</sub> shell formation through the slow thermal decomposition of EDTA at high temperature, which resulted in Bi<sub>2</sub>WO<sub>6</sub> precipitation around the UCNP core. This novel composite thus approaches the optimal utilization of UV-vis-NIR photons, thereby contributing effectively to the development of active solar photocatalysts.

Bisphenol A (BPA) is an endocrine-disrupting compound. The presence of BPA in urine, breast milk, human serum, placental tissue, and umbilical cord blood is well documented [30]. It enters environmental compartments as a contaminant during its manufacture, transport, and processing. BPA-based products also contaminate water bodies during environmental degradation [31]. In this research, we investigated the synthesis, upconversion capacity, and photocatalytic performance of the UCNP@Bi<sub>2</sub>WO<sub>6</sub> nanocomposite for BPA degradation.

## 2. Experimental

### 2.1. Synthesis of NaYF<sub>4</sub>: Yb<sup>3+</sup>, Gd<sup>3+</sup>, Tm<sup>3+</sup> (UCNP core)

Eighty milliliters of 1.35 M trisodium citrate solution was prepared in deionized (DI) water. Y(NO<sub>3</sub>)<sub>3</sub>·6H<sub>2</sub>O (2.8 mmol), Yb(NO<sub>3</sub>)<sub>3</sub>·5H<sub>2</sub>O

(0.72 mmol), Gd(NO<sub>3</sub>)<sub>3</sub>·6H<sub>2</sub>O (0.4 mmol), and Tm(NO<sub>3</sub>)<sub>3</sub>·5H<sub>2</sub>O (0.08 mmol) were mixed and slowly added to the trisodium citrate solution. NaF (36 mmol) was added to the solution under vigorous stirring. After stirring for 30 min, the solution was transferred to a 140-mL Teflon-lined stainless-steel vessel. Hydrothermal reaction was carried out at 200 °C for 2 h. The white precipitates were separated by centrifuging at 6000 rpm for 10 min. The citrate-capped UCNPs were washed with DI water and methanol. Then, they were dried at 60 °C for 12 h.

### 2.2. Synthesis of the UCNP@Bi<sub>2</sub>WO<sub>6</sub> nanocomposite

One millimole each of Bi(NO<sub>3</sub>)<sub>3</sub>·5H<sub>2</sub>O and Na<sub>2</sub>WO<sub>4</sub>·2H<sub>2</sub>O were added to 40 mL of 20% HNO<sub>3</sub> solution. The suspension was stirred for 4 h at room temperature. Four millimoles of EDTA were added to the suspension and stirred for 15 min. Then, the suspension was transferred to a round-bottom flask and heated at 90 °C on a heating mantle for complete EDTA dissolution. Water was evaporated by heating. The products were washed with water and ethanol. Subsequently, they were dried at 60 °C for 12 h. The EDTA-metal complexes were dissolved in 80 mL of DI water. The pH was adjusted to 7.5 using NaOH. The metal complexes did not precipitate at this pH because they were stabilized with EDTA. H<sub>2</sub>O<sub>2</sub> (16 mmol) and urea (32 mmol) were slowly added to the EDTA-metal complex solution. After 30 min of stirring, 100 mg of the citrate-capped UCNPs were added, and the solution was autoclaved at 180 °C for 12 h. The EDTA decomposed at that high temperature, and the Bi<sub>2</sub>WO<sub>6</sub> nanoparticles were assembled around the UCNP core. After the hydrothermal reaction, the product was centrifuged, washed with ethanol and water, and dried at 60 °C overnight. The nanocomposite was finally calcined at 450 °C for 4 h.

The UCNP and EDTA-Bi<sub>2</sub>WO<sub>6</sub> complexes exist in a homogenous suspension at room temperature. Shell growth around the UCNP core can be divided into three stages (Fig. 1). EDTA is thermally degraded at a reaction temperature of 150 °C, and Bi<sub>2</sub>WO<sub>6</sub> starts to crystallize in the reaction mixture at stage 1. The thermal disintegration of EDTA-Bi<sub>2</sub>WO<sub>6</sub> was tested at 120 °C, 130 °C, and 140 °C. Little/no crystallization, however, occurred in the reaction vessel below 150 °C. Heating at 150 °C for 12 h results in little Bi<sub>2</sub>WO<sub>6</sub> deposition, which suggests that a high temperature is required for uniform shell formation (Fig. S2(a)). Stage 2 starts at 180 °C and results in the deposition of Bi<sub>2</sub>WO<sub>6</sub> particles on hexagonal UCNPs. UCNPs act as nucleation centers/seeds for adsorption of Bi<sub>2</sub>WO<sub>6</sub> molecules. This heterogenous nucleation results in preferential growth of Bi<sub>2</sub>WO<sub>6</sub> around the UCNP core. The growth and thickness of Bi<sub>2</sub>WO<sub>6</sub> shell are controlled in Stage 3. The optimal thickness of 30 nm was achieved in 12 h. The Bi<sub>2</sub>WO<sub>6</sub> shell continues to grow until it reaches a maximum thickness of 85 nm (Fig. S2(b)). After that, the core@shell structure becomes unstable and starts to disintegrate (Fig. S2(c)).

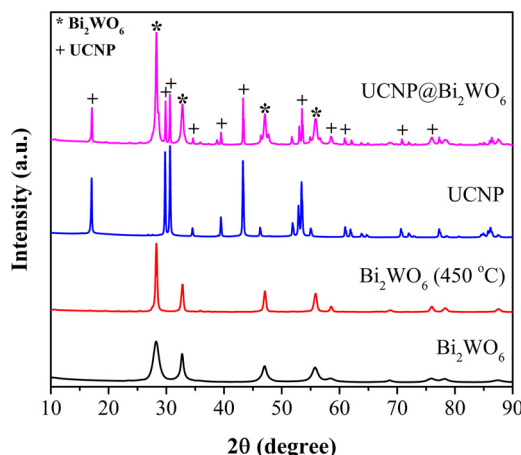


Fig. 2. XRD spectra of  $\text{Bi}_2\text{WO}_6$ , UCNP, and UCNP@ $\text{Bi}_2\text{WO}_6$ .

### 3. Results and discussion

#### 3.1. XRD

Fig. 2 shows the XRD patterns of the  $\text{Bi}_2\text{WO}_6$ , UCNP, and UCNP@ $\text{Bi}_2\text{WO}_6$  used in this research. Four distinct peaks at  $2\theta = 28.3^\circ$ ,  $32.7^\circ$ ,  $47^\circ$ , and  $55.7^\circ$  are characteristic of the perovskite phase of  $\text{Bi}_2\text{WO}_6$  (JCPDS No. 75-3514). Those peak positions indicate that crystal growth occurred along the (131), (200), (202), and (133) planes of  $\text{Bi}_2\text{WO}_6$  [32]. Broad peaks in the as-synthesized  $\text{Bi}_2\text{WO}_6$  imply low crystallinity. To improve the crystalline phase, we calcined  $\text{Bi}_2\text{WO}_6$  at three different temperatures,  $350^\circ\text{C}$ ,  $450^\circ\text{C}$ , and  $550^\circ\text{C}$  (Fig. S4). The peaks were sharper and more intense at higher calcination temperatures, suggesting an increase in the crystalline phase. However, the peak intensity declined at temperatures higher than  $450^\circ\text{C}$ , possibly due to the sintering effect at  $550^\circ\text{C}$ , which resulted in the fusion of crystal boundaries [33]. Thus, all composites were calcined at  $450^\circ\text{C}$  in this research. The XRD spectra of UCNPs in Fig. 2 exhibit peaks at  $2\theta = 17^\circ$  (100),  $29.78^\circ$  (110),  $30.63^\circ$  (101),  $34.52^\circ$  (200),  $39.4^\circ$  (111),  $43.26^\circ$  (201),  $46.23^\circ$  (210),  $51.86^\circ$  (002),  $52.88^\circ$  (300),  $53.41^\circ$  (211),  $54.99^\circ$  (102),  $60.96^\circ$  (112),  $61.89^\circ$  (220),  $70.64^\circ$  (311), and  $77.25^\circ$  (302). Those peaks can be attributed to the hexagonal  $\beta$ -phase of  $\text{NaYF}_4$  (JCPDS No. 77-2042). No peaks corresponding to the  $\text{NaYF}_4$  cubic phase ( $2\theta = 27.95^\circ$ ,  $32.72^\circ$ , and  $46.9^\circ$ ) were observed, indicating that the UCNPs existed only in the hexagonal form [34,35]. The XRD spectrum of UCNP@ $\text{Bi}_2\text{WO}_6$  exhibited the peaks of both UCNP and  $\text{Bi}_2\text{WO}_6$ , showing that core@shell nanoparticles were successfully synthesized. The absence of any extraneous peaks in the XRD spectra confirms the crystalline purity of the synthesized composites. The crystallite sizes of  $\text{Bi}_2\text{WO}_6$  and UCNP, determined from Scherrer's equation, were 7.8 and 345.7 nm, respectively.

#### 3.2. Structure and morphology

The surface and internal structure were investigated using TEM, SEM, HRTEM, and EDS-mapping. Fig. 3(a) shows the SEM image of the hexagonal UCNPs with a uniform diameter of 300–350 nm. Plate-like UCNPs formed with distinct edges and few surface defects. Their average thickness was 110–130 nm. TEM image of the UCNPs in Fig. 3(b) further confirm their excellent geometrical features with symmetrical boundaries. The size of the UCNPs determined by SEM and TEM is consistent with that calculated using Scherrer's equation using XRD. The  $\text{Bi}_2\text{WO}_6$  shell assembled around the UCNP core via hydrothermal treatment is shown in Fig. 3(c). The UCNPs were uniformly enveloped by the  $\text{Bi}_2\text{WO}_6$  particles, and unbound shell particles were little to none (Figs. 3(c and d)). The thickness of the  $\text{Bi}_2\text{WO}_6$  shell was 25–30 nm (Fig. 3(e)), which is ideal for transmitting NIR to UCNP core.

Higher shell transmittance is vital to effective photon upconversion for catalytic applications. Interfacial connection and crystallographic features of the UCNP@ $\text{Bi}_2\text{WO}_6$  composite were investigated with HRTEM. Fig. 3(f) reveals two distinct types of lattice fringes in the composite structure. The interplanar spacing of 0.31 nm corresponds to the (131) plane of  $\text{Bi}_2\text{WO}_6$ , whereas the larger lattice spacing indicates the presence of a (100) plane of hexagonal  $\text{NaYF}_4$ . The HRTEM results are consistent with those of XRD, confirming the crystallinity of the composite [36,37]. The spatial distribution of elements in the UCNP@ $\text{Bi}_2\text{WO}_6$  composite is illustrated in Fig. 3(g–l). The relative abundance of elements is consistent with the intended percentage composition of UCNP@ $\text{Bi}_2\text{WO}_6$ . The densest image was formed in yttrium due to its presence in the core as the host matrix (70%). Gadolinium and ytterbium were present alongside the yttrium atoms to the extent of 20 and 18%, respectively.  $\text{Bi}_2\text{WO}_6$  shell formation was also confirmed by the presence of bismuth and tungsten at the surface of the hexagonal UCNP particles (Figs. 3(k and l)).

#### 3.3. Functional groups

The FT-IR spectra are shown in Fig. 4. The absorption signals at  $3200$ – $3500\text{ cm}^{-1}$  in  $\text{Bi}_2\text{WO}_6$ ,  $\text{Bi}_2\text{WO}_6$ -EDTA, and the UCNPs correspond to the symmetric O–H stretching vibrations of hydroxyl groups. Similarly, the absorption between  $1050$  and  $1450\text{ cm}^{-1}$  in the FT-IR spectra is caused by the O–H bending vibrations, C–O–C stretching, and C–O vibrations of hydrocarbons [38]. The peak intensities at  $3200$ – $3500$  and  $1050$ – $1450\text{ cm}^{-1}$  decreased in the calcined composites, indicating the removal of O–H groups, adsorbed water molecules, and organic impurities. The broad absorption band in the  $\text{Bi}_2\text{WO}_6$ -EDTA spectrum near  $2400$ – $3400\text{ cm}^{-1}$  could result from the hydrolysis of EDTA to its acid form [39]. The  $\text{Bi}_2\text{WO}_6$ -EDTA spectrum showed carbonyl ( $\text{C}=\text{O}$ ) and  $\text{C}=\text{C}$  groups at  $1740$  and  $1600\text{ cm}^{-1}$ , respectively. The absorption peaks associated with EDTA functional groups were absent/weakened in the  $\text{Bi}_2\text{WO}_6$  spectrum, possibly because of the disintegration of  $\text{Bi}_2\text{WO}_6$ -EDTA complexes followed by the decomposition of EDTA during the high-temperature hydrothermal treatment [40]. Splitting of the EDTA-metal complexes corroborated our synthesis approach for *in situ* assembly of the  $\text{Bi}_2\text{WO}_6$  shell around the UCNP core. The absorption peak at  $700$ – $800\text{ cm}^{-1}$ , which is the characteristic absorption band of the W–O and Bi–O groups, appeared in spectra of the composites containing  $\text{Bi}_2\text{WO}_6$  [41]. This peak shifted toward a lower wavenumber in the  $\text{Bi}_2\text{WO}_6$ -EDTA spectrum, confirming the coordination between EDTA and  $\text{Bi}_2\text{WO}_6$  [42]. The peaks at  $1590$  and  $1395\text{ cm}^{-1}$  in UCNP spectrum correspond to COO asymmetric stretch and  $\text{CH}_2$  flexural vibrations [43]. The presence of these functional groups indicates successful capping of the UCNPs with citrate ligands. The characteristic absorption peak of  $\text{NaYF}_4$  appeared at around  $450\text{ cm}^{-1}$  in UCNP-containing spectra. The citrate and EDTA functional groups were mostly decomposed during the hydrothermal reaction between the UCNPs and  $\text{Bi}_2\text{WO}_6$ , as shown in the UCNP@ $\text{Bi}_2\text{WO}_6$  spectrum. In the calcined UCNP@ $\text{Bi}_2\text{WO}_6$  spectrum, only the characteristic absorption peaks of UCNPs and  $\text{Bi}_2\text{WO}_6$  were observed. The remaining peaks associated with organic functional groups and impurities were eliminated during calcination.

#### 3.4. XPS

We performed XPS analysis to understand the elemental states and chemical coordination between the UCNP core and  $\text{Bi}_2\text{WO}_6$  shell. Fig. 5(a) shows the  $\text{Bi}4f$  spectrum of  $\text{Bi}_2\text{WO}_6$ , with the peaks at  $158.9$  and  $163.9\text{ eV}$  confirming the presence of bismuth in the  $\text{Bi}^{3+}$  oxidation state [44]. The binding energy (BE) peaks of  $\text{Bi}4f_{7/2}$  and  $\text{Bi}4f_{5/2}$  increased by 1 eV when  $\text{Bi}_2\text{WO}_6$  was assembled around the UCNP core. This shift in the BE peaks could be caused by the formation of Bi–O–Y bonds in the UCNP@ $\text{Bi}_2\text{WO}_6$  composite. The absence of peaks at  $156.5$  and  $162\text{ eV}$ , associated with elemental bismuth ( $\text{Bi}^0$ ), indicates that the

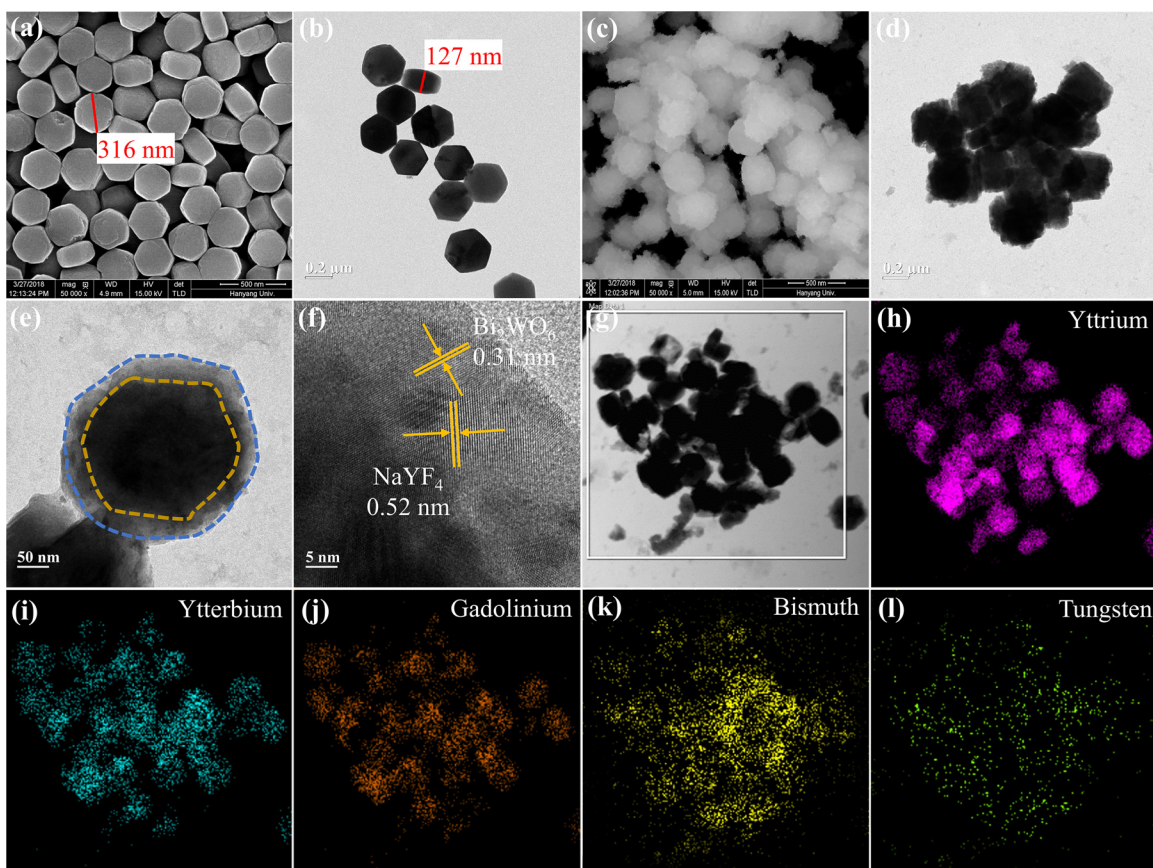


**Fig. 3.** (a) SEM and (b) TEM images of UCNP. (c) SEM and (d) TEM images of UCNP@Bi<sub>2</sub>WO<sub>6</sub>. (e) TEM image of a single UCNP@Bi<sub>2</sub>WO<sub>6</sub> particle. (f) HRTEM image of UCNP@Bi<sub>2</sub>WO<sub>6</sub> composite showing lattice fringe spacing of Bi<sub>2</sub>WO<sub>6</sub> and NaYF<sub>4</sub>. (g) TEM sample used for energy-dispersive X-ray spectroscopy (EDS mapping). (h–l) EDS mapping showing spatial distribution and relative abundance of elements in UCNP@Bi<sub>2</sub>WO<sub>6</sub>.

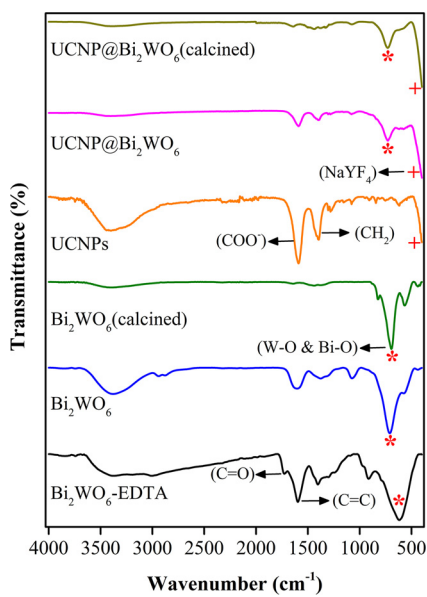


**Fig. 4.** FT-IR spectra illustrating important functional groups.

bismuth precursor was completely converted to Bi<sub>2</sub>WO<sub>6</sub> [45]. The host matrix in the UCNP core, yttrium, revealed two BE peaks at 302.2 and 314.8 eV (Fig. 5(b)). These BE peaks correspond to the Y<sup>3+</sup> oxidation state [46]. The electronic environment of the NaYF<sub>4</sub> core changed after the deposition of the Bi<sub>2</sub>WO<sub>6</sub> shell. The shift in BE peaks of Y<sup>3+</sup> and Y<sup>3+</sup>/

indicates that bismuth and tungsten atoms were successfully incorporated in the host NaYF<sub>4</sub> lattice. The BE peaks at 182.7 and 186.3 eV in Fig. 5(c) are associated with Yb<sup>3+</sup> [47,48]. Likewise, the Gd<sup>3d<sub>3/2</sub></sup> and Gd<sup>3d<sub>5/2</sub></sup> spin-orbit splitting at 1187 and 1219 eV confirms the Gd<sup>3+</sup> oxidation state in the UCNP@Bi<sub>2</sub>WO<sub>6</sub> composite [49]. Fig. 5(d) shows the deconvoluted spectra of O1s, which yielded two distinct peaks at 530.9 and 532.5 eV. The two O1s peaks reflect the presence of multiple oxygen states in UCNP@Bi<sub>2</sub>WO<sub>6</sub>. The peak at 530.9 eV corresponds to oxygen bonded to metals, whereas that at 532.5 eV can be attributed to oxygen species in adsorbed water molecules. The shifting BE peaks in bismuth and yttrium, along with the multiple oxygen states, implies that the Bi<sub>2</sub>WO<sub>6</sub> shell was chemically bonded with the UCNP core through electron sharing. The oxidation states of elements indicated the successful synthesis of the composite, and absence of metallic species bodes well for photochemical reactions. The complete XPS survey spectrum of the UCNP@Bi<sub>2</sub>WO<sub>6</sub> composite is shown in Fig. S5.

### 3.5. Light-harvesting capacity

We explored the light absorption, photon-upconversion, charge-carrier separation, and photocurrent response of the UCNP@Bi<sub>2</sub>WO<sub>6</sub> nanocomposite under solar and NIR illumination. First, we examined the optical properties of the composite using diffuse reflectance spectroscopy (DRS), as shown in Fig. 6(a). The Bi<sub>2</sub>WO<sub>6</sub> shell exhibited strong photoabsorption in the UV-vis region, suggesting that it can utilize the direct solar photons as well as the upconverted infrared photons. The strong absorption signal around 500 nm corresponds to the band-gap energy of Bi<sub>2</sub>WO<sub>6</sub>, which was calculated using the Tauc equation [50]:

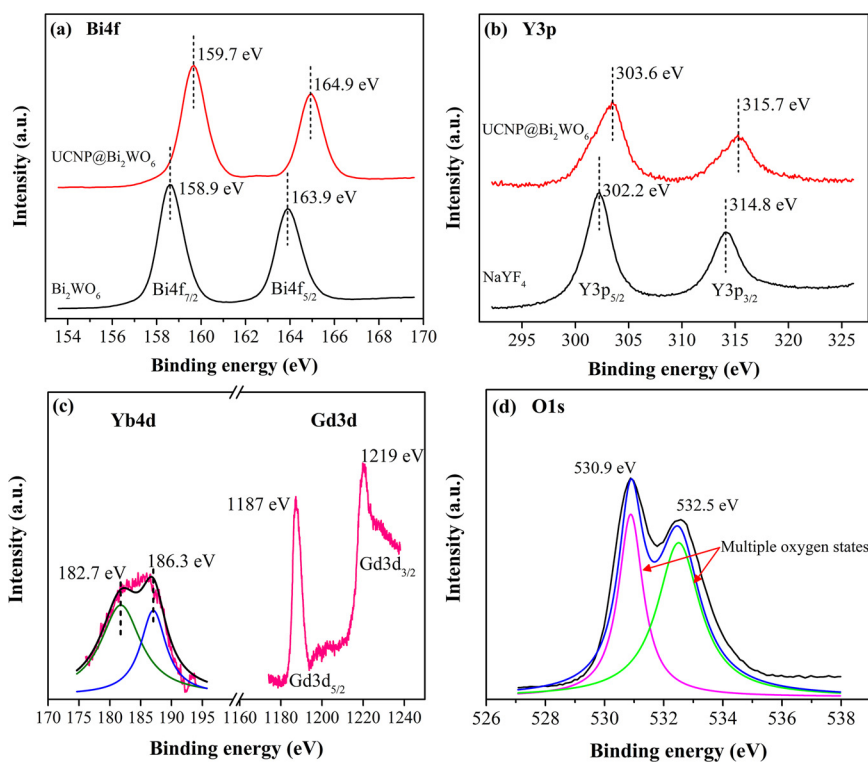


Fig. 5. XPS spectra of (a) Bi4f, (b) Y3p, (c) Yb4d and Gd3d, and (d) O1s.

$$(\hbar\alpha)1/n = A(\hbar\nu - E_g), \quad (1)$$

where  $h$  is Planck's constant,  $\nu$  is the vibrational frequency,  $\alpha$  is the absorption coefficient,  $n$  refers to the type of electron transition ( $n = 1/2$  for direct transitions),  $E_g$  is the band-gap energy, and  $A$  is a proportionality constant.  $\alpha$  is directly proportional to the Kubelka-Munk function ( $F(R\infty)$ ) [51]. Substituting  $F(R\infty)$  in Eq. 1 gives:

$$(\hbar\nu F(R\infty))^2 = A(\hbar\nu - E_g). \quad (2)$$

The band-gap energies of  $\text{Bi}_2\text{WO}_6$  and  $\text{UCNP}@\text{Bi}_2\text{WO}_6$ , calculated by projecting the cutoff-tangent to the x-axis, were 2.63 and 2.49 eV, respectively (Fig. 6(a-inset)). Low band gap energy and high absorption in UV-vis region implies that  $\text{UCNP}@\text{Bi}_2\text{WO}_6$  can utilize photons in a wide light spectrum, which results in higher quantum yield for

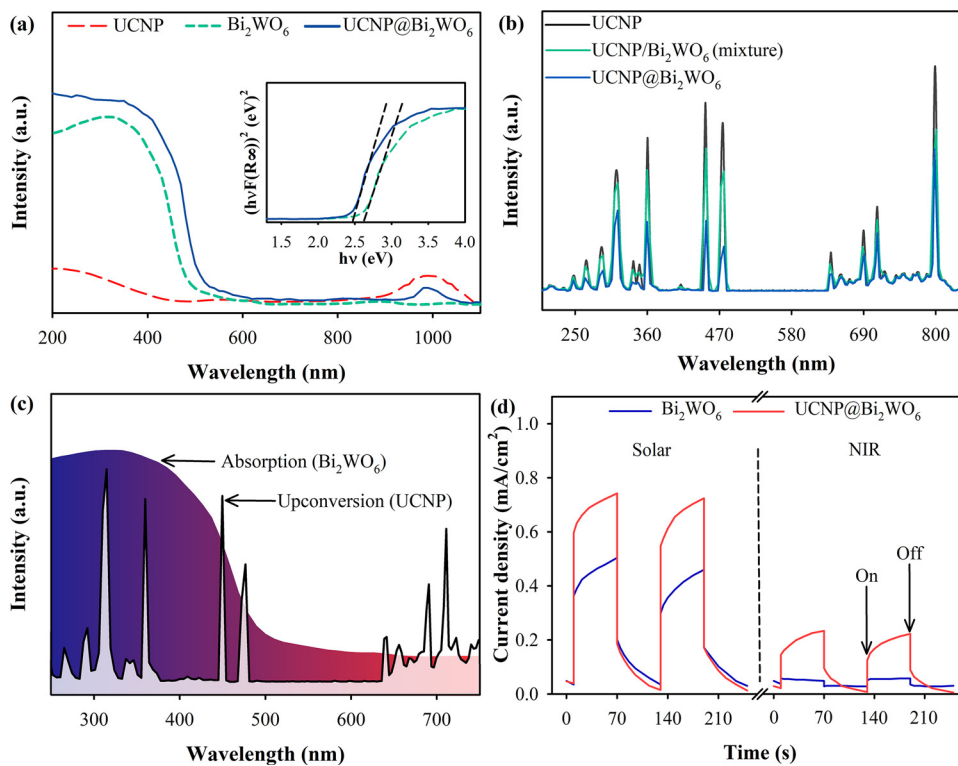


Fig. 6. (a) UV-vis-NIR absorption spectra of the nanocomposites. Inset shows the Tauc plot to determine the band-gap energy. (b) Photoluminescence spectra of the UCNPs, UCNP@ $\text{Bi}_2\text{WO}_6$ , and UCNP@ $\text{Bi}_2\text{WO}_6$  (mixture). (c) Absorption and emission spectral overlap of the  $\text{Bi}_2\text{WO}_6$  shell and UCNP core. (d) Photocurrent responses of the  $\text{Bi}_2\text{WO}_6$  and UCNP@ $\text{Bi}_2\text{WO}_6$  to light on-off cycles under solar and NIR light.

**Table 1**Upconversion emissions and corresponding transitions of  $\text{Tm}^{3+}$  and  $\text{Gd}^{3+}$  ions.

Activator	Transition type	UC emissions (nm)	Corresponding transitions
$\text{Tm}^{3+}$	Two-photon	799, 690	$^3\text{H}_4 \rightarrow ^3\text{H}_6$ , $^3\text{F}_3 \rightarrow ^3\text{H}_6$
	Three-photon	644, 475	$^1\text{G}_4 \rightarrow ^3\text{H}_6$ , $^1\text{G}_4 \rightarrow ^3\text{F}_4$
	Four-photon	449, 360	$^1\text{D}_2 \rightarrow ^3\text{H}_6$ , $^1\text{D}_2 \rightarrow ^3\text{F}_4$
	Five-photon	339, 290	$^1\text{I}_6 \rightarrow ^3\text{H}_6$ , $^1\text{I}_6 \rightarrow ^3\text{F}_4$
$\text{Gd}^{3+}$		313, 267	$^6\text{P}_{7/2} \rightarrow ^8\text{S}_{7/2}$ , $^6\text{I}_{7/2} \rightarrow ^8\text{S}_{7/2}$

photoreactions. The decrease in band-gap energy is due to a red shift in the absorption edge caused by the large core@shell structure and the doping-induced lattice strain [52]. The absorption spectrum of the UCNPs exhibited moderate absorption in the UV and NIR regions, which corroborated the upconversion mechanism. The absorption between 900 and 1050 nm, associated with the  $^2\text{F}_{7/2} \rightarrow ^2\text{F}_{5/2}$  transition, is a characteristic absorption range for  $\text{Yb}^{3+}$  ions [53]. The NIR absorption of the UCNPs core was preserved in the UCNPs@ $\text{Bi}_2\text{WO}_6$  composite. The transfer of IR photons via  $\text{Bi}_2\text{WO}_6$  shell to UCNPs core substantiated the suitability of using  $\text{Bi}_2\text{WO}_6$  as a transmitting shell. Overall, the combination of the active core and inert photocatalyst shell yielded a hybrid composite with excellent photoresponse properties in the solar spectrum.

We investigated the photon-upconversion potential of the as-synthesized composites with photoluminescence spectroscopy (PL), as shown in Fig. 6(b). The emission bands in the blue (250–400 nm), green (450–600 nm), and red (650–800 nm) regions confirmed the upconversion of NIR photons to UV-vis photons. The emission spectrum of  $\text{Tm}^{3+}$  can be divided into four groups (Table 1). The emissions at 799 and 690 nm were generated by a two-photon transition from the  $^3\text{F}_3$  and  $^3\text{H}_4$  states, respectively. The three-photon transition process in the  $^1\text{G}_4$  group produced peaks at 644 and 475 nm. The emission in the blue region resulted from four- and five-photon transitions from the  $^1\text{D}_2$  and  $^1\text{I}_6$  states, respectively [54,55]. Many emission peaks from  $\text{Yb}^{3+}$ – $\text{Tm}^{3+}$  pairs are caused by the ladder-like structure of energy levels in  $\text{Tm}^{3+}$ , which increases the probability of multi-photon transitions. These peaks are difficult to achieve using other sensitizers–activator combinations because of their dense energy levels and inefficient non-radiative transitions [22]. The strong UV emission at 313 nm occurred due to the  $\text{Gd}^{3+}$  ions in the UCNPs structure. Because of the large energy difference between the ground ( $^8\text{S}_{7/2}$ ) and excited states ( $^6\text{P}_1$ ), it is not possible for 980-nm photons to excite the  $\text{Gd}^{3+}$  ions. However, the excited states of  $\text{Gd}^{3+}$  were filled via an electron transition from  $^3\text{P}_2$  ( $\text{Tm}^{3+}$ ) to  $^6\text{I}_J$  ( $\text{Gd}^{3+}$ ) [56].

Light absorption and photon-upconversion can enhance catalytic activity if they interact constructively. To investigate the mutual collaboration between the above-mentioned properties, we overlapped the  $\text{Bi}_2\text{WO}_6$  absorption spectrum with the UCNPs emission spectrum (Fig. 6(c)). The wavelength of photons emitted from the UCNPs corresponds to the light absorption range of  $\text{Bi}_2\text{WO}_6$ . Therefore, the unique core@shell combination described here provides the spectral overlapping essential to the energy transfer process between the core and shell.

Energy transfer from the UCNPs core to the photocatalyst shell was explored by comparing the PL intensities of UCNPs, UCNPs@ $\text{Bi}_2\text{WO}_6$ , and UCNPs@ $\text{Bi}_2\text{WO}_6$  (mixture) (Fig. S6). The highest PL emission was exhibited by the UCNPs, and it decreased after the formation of the  $\text{Bi}_2\text{WO}_6$  shell. In the UCNPs@ $\text{Bi}_2\text{WO}_6$  spectrum, the reductions in blue, green, and red emissions were 38%, 61%, and 11%, respectively. The marked 61% decline is caused by the overlapping of absorption band of  $\text{Bi}_2\text{WO}_6$  with green emissions from UCNPs core. The decrease in PL in the mixture of UCNPs and  $\text{Bi}_2\text{WO}_6$  was smaller, 11% and 5% in green and red emissions, respectively. These results confirmed non-radiative energy transfer, or Förster resonance energy transfer (FRET), from the UCNPs core to the  $\text{Bi}_2\text{WO}_6$  shell. FRET is an excellent, non-radiative method for transferring energy from donor to acceptor molecules. It

requires a distance of less than 10 nm between the donor and acceptor, which we achieved by growing the  $\text{Bi}_2\text{WO}_6$  shell directly over the UCNPs core [57,58]. The absorption–emission spectral overlapping and close interfacial contact promoted FRET in the UCNPs@ $\text{Bi}_2\text{WO}_6$ . On the contrary, the large donor–acceptor distance in the UCNPs@ $\text{Bi}_2\text{WO}_6$  (mixture) resulted in conventional radiative energy transfer. Due to this inefficient energy transfer, the PL intensity of the powder mixture of UCNPs and  $\text{Bi}_2\text{WO}_6$  was higher than that of the closely bound core–shell arrangement in the UCNPs@ $\text{Bi}_2\text{WO}_6$ .

Potentiometric experiments were performed to investigate the charge–carrier separation in the composites (Fig. S7). The lower open circuit potential ( $V_{OC}$ ) corresponds to better charge–carrier separation across heterojunctions [59]. The  $V_{OC}$  of  $\text{Bi}_2\text{WO}_6$ , UCNPs@ $\text{Bi}_2\text{WO}_6$ , and UCNPs@ $\text{Bi}_2\text{WO}_6$  (mixture) was  $-0.24$ ,  $-0.49$ , and  $-0.33$  V, respectively. Doping  $\text{Bi}_2\text{WO}_6$  with UCNPs suppressed charge–carrier recombination, which was more pronounced in the core@shell composite than the mixture of UCNPs and  $\text{Bi}_2\text{WO}_6$ . Electron–hole separation in UCNPs@ $\text{Bi}_2\text{WO}_6$  is imperative for catalytic applications. Fig. 6(d) shows the photoresponse performance of the synthesized composites under solar and NIR radiation. A photocurrent was generated in response to photon energy received during light cycles, which was reverted to zero in subsequent dark cycles.  $\text{Bi}_2\text{WO}_6$  was inactive under NIR before its combination with the UCNPs. The photocurrent density of the UCNPs@ $\text{Bi}_2\text{WO}_6$  was  $0.22 \text{ mA/cm}^2$  under NIR, which improved 3.5 times under solar radiation. The current densities of  $\text{Bi}_2\text{WO}_6$  and UCNPs@ $\text{Bi}_2\text{WO}_6$  were  $0.43$  and  $0.78 \text{ mA/cm}^2$ , respectively. Thus, combining a UCNPs core with a  $\text{Bi}_2\text{WO}_6$  catalyst accounted for a 1.8-fold increase in the photoresponse under solar radiation. The applications of the nanocomposite explored in this research can be extended to photoelectrochemical water splitting and photocatalytic hydrogen production using natural sunlight.

### 3.6. BPA degradation

We evaluated the photocatalytic activity of the UCNPs@ $\text{Bi}_2\text{WO}_6$  composite using BPA photodegradation under simulated solar and NIR radiation. As shown in Fig. 7(a), the BPA concentration dropped continuously as the reaction proceeded from 0 to 180 min in the presence of the photocatalysts.  $\text{Bi}_2\text{WO}_6$  and the UCNPs exhibited 65% and 2% BPA degradation in 180 min, respectively. Degradation reached 94% under solar illumination when the UCNPs@ $\text{Bi}_2\text{WO}_6$  composite was used. The additional increase of 29% from  $\text{Bi}_2\text{WO}_6$  to UCNPs@ $\text{Bi}_2\text{WO}_6$  is associated with the enhanced use of solar light through the upconversion of unused NIR photons into active UV-vis photons. The increase in UV-vis photon population was also reflected by a two-fold increase in reaction kinetics. The observed pseudo-first-order rates were  $0.0029$ ,  $0.088$ ,  $0.1$ , and  $0.19 \text{ min}^{-1}$  for the UCNPs,  $\text{Bi}_2\text{WO}_6$ , UCNPs@ $\text{Bi}_2\text{WO}_6$  (mixture), and UCNPs@ $\text{Bi}_2\text{WO}_6$ , respectively (Fig. S8). Energy transfer from the core to the shell was investigated by comparing the performance of the UCNPs@ $\text{Bi}_2\text{WO}_6$  with that of the mixture of the UCNPs and  $\text{Bi}_2\text{WO}_6$  catalyst. The former showed 21% higher BPA degradation, substantiating the non-radiative energy transfer between the core and shell. The low performance of the UCNPs@ $\text{Bi}_2\text{WO}_6$  (mixture) can be attributed to the energy loss caused by the radiative energy transfer between donor and acceptor molecules.

Photon upconversion and its role in enhancing photocatalytic activity was verified by our test of BPA degradation under NIR radiation (Fig. 7(b and c)). Taken alone, NIR radiation, UCNPs, and  $\text{Bi}_2\text{WO}_6$  failed to degrade BPA.  $\text{Bi}_2\text{WO}_6$  exhibited BPA degradation with solar radiation, but it was inactive under NIR. Photodegradation with NIR was observed when  $\text{Bi}_2\text{WO}_6$  was combined with the UCNPs. The upconverted NIR photons were used by both the UCNPs@ $\text{Bi}_2\text{WO}_6$  and UCNPs@ $\text{Bi}_2\text{WO}_6$  (mixture) to degrade 51% and 26% of BPA, respectively, in 10 h. The reaction rates under NIR were much slower than those observed under solar radiation. For example, the reaction rate with UCNPs@ $\text{Bi}_2\text{WO}_6$  was 190 times higher under solar radiation than NIR

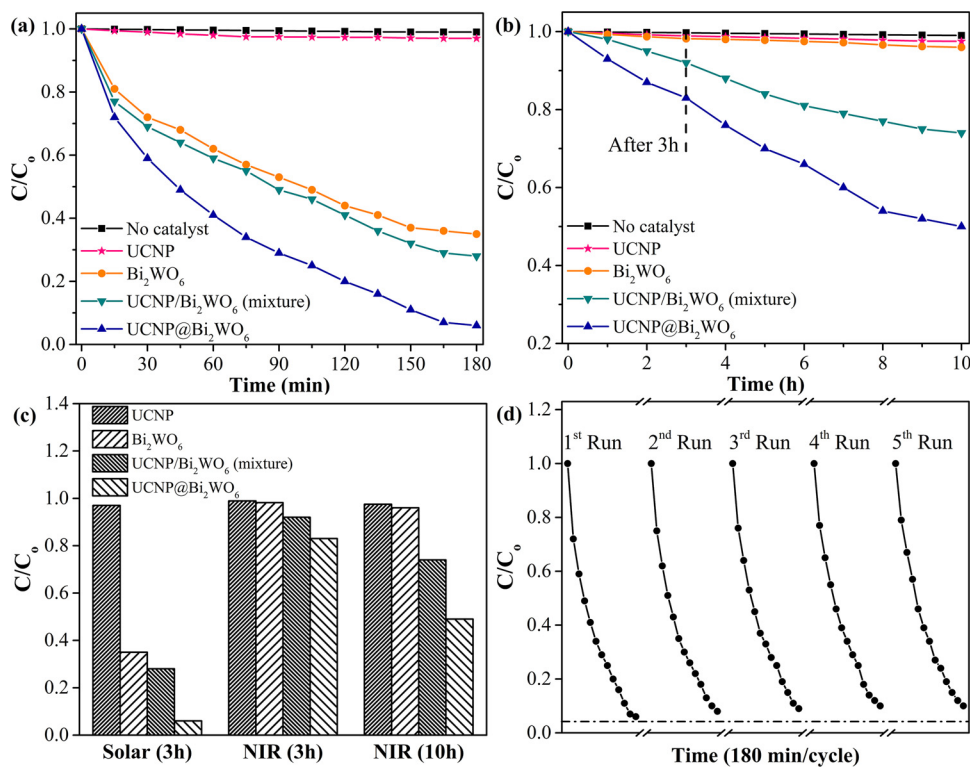


**Fig. 7.** Photocatalytic performance of composites under (a) solar and (b) NIR irradiation. (c) Comparison of BPA degradation under visible spectrum and NIR radiation by various composites. (d) Photocatalytic degradation of BPA in five consecutive cycles under solar irradiation.

because of the ability to exploit UV-vis as well as NIR photons.

The stability and reusability of UCNP@Bi<sub>2</sub>WO<sub>6</sub> nanocomposite are important for practical applications. We demonstrated the photoactivity of recycled composites for five successive BPA degradation cycles, as shown in Fig. 7(d). The photocatalyst, with a 5% difference from the first run, exhibited 89% BPA degradation after the fifth cycle. Thus, the UCNP@Bi<sub>2</sub>WO<sub>6</sub> composite is reusable and is not deactivated by extended exposure to UV-vis-NIR radiation. The structural stability of the composite was investigated by XRD, FT-IR, and XPS analyses of the recycled catalyst (Fig. S9). The XRD spectra of the pure and recovered composite were almost identical, with only minor changes in peak heights. Peaks at 20 = 37°, 45°, and 49°, corresponding to elemental bismuth were not observed, which confirmed the integrity of the Bi<sub>2</sub>WO<sub>6</sub> shell [60]. The FT-IR spectra did not exhibit any redundant absorption peaks. The peaks associated with the inter-band transitions of bismuth (990–1100 cm<sup>-1</sup>) were absent [61]. The stability of Bi<sub>2</sub>WO<sub>6</sub> was further substantiated by the XPS spectra shown in Fig. S9(c). The binding energy of Bi4f<sub>7/2</sub> and Bi4f<sub>5/2</sub> was the same in the pure and recycled photocatalysts. The absence of peaks at 156.5 and 162 eV, associated with elemental bismuth (Bi<sup>0</sup>), indicated that bismuth sustained the photocatalytic reactions.

### 3.7. Photocatalytic mechanism

The reaction mechanism of this novel UCNP@Bi<sub>2</sub>WO<sub>6</sub> composite is illustrated in Fig. 8. Bi<sub>2</sub>WO<sub>6</sub> with a narrow band gap (2.49 eV) is activated directly by solar illumination and indirectly by upconverted photons from the UCNP core. Upon irradiation, the sensitizer (Yb<sup>3+</sup>) gets excited and transfers energy to the activators (Gd<sup>3+</sup> and Tm<sup>3+</sup>) through dipole-dipole resonant interactions [22]. Subsequently, the activators are relaxed non-radiatively and give energy to their neighboring Bi<sub>2</sub>WO<sub>6</sub> catalyst molecules. The non-radiative energy transfer is much more efficient than the conventional radiative process, which suffers from inevitable energy loss. However, non-radiative energy transfer demands sufficient spectral overlap and minimal distance

between the donsor and acceptor [62]. The novel design of the core@shell composite in this study meets both those conditions. The absorption band of Bi<sub>2</sub>WO<sub>6</sub> overlaps with the emissions from the UCNP core in the UV-vis range (Fig. 6(c)), and direct growth of the Bi<sub>2</sub>WO<sub>6</sub> over the UCNP core makes the donor–acceptor distance negligible. This appropriate spectral overlap and close donor–acceptor contact form the basis for non-radiative energy transfer between the core and shell.

Radical scavenging experiments were performed to investigate the role of reactive oxygen species (ROS) in BPA photodegradation. As shown in Fig. S10, BPA degradation was significantly suppressed by TBA, suggesting a strong involvement of hydroxyl radicals (·OH) in the photochemical reaction. By contrast, 65% of the BPA was degraded in the presence of BQ, a trapping agent for the superoxide radical (·O<sub>2</sub><sup>-</sup>). The scavenging experiments thus imply the major role of ·OH radicals in BPA degradation. To better understand ROS generation by the Bi<sub>2</sub>WO<sub>6</sub> photocatalyst, we determined the conduction band (CB) and valence band (VB) edge potentials using Butler and Ginley's method [63]:

$$E_{VB} = X - E^e + 0.5E_g \quad (3)$$

$$E_{CB} = E_{VB} - E_g, \quad (4)$$

where E<sub>CB</sub> is the CB potential, E<sub>VB</sub> is the VB potential, E<sup>e</sup> is the energy of electrons versus the hydrogen scale (4.5 eV), E<sub>g</sub> is the band-gap energy, and X is the absolute electronegativity of Bi<sub>2</sub>WO<sub>6</sub>. The theoretically calculated VB and CB edge potentials were verified experimentally using ultraviolet photoelectron spectroscopy (Fig. S11). The ·OH radicals are produced at the VB of Bi<sub>2</sub>WO<sub>6</sub> because its VB potential (2.7 eV) is higher than the H<sub>2</sub>O/·OH redox potential (2.4 eV). The scavenging experiments indicate the presence of ·O<sub>2</sub><sup>-</sup> radicals; however, the CB edge potential of Bi<sub>2</sub>WO<sub>6</sub> (0.21 eV) is not low enough for O<sub>2</sub>/·O<sub>2</sub><sup>-</sup> conversion (-0.05 eV). Based on the results of radical trapping and band edge calculations, we propose an indirect two-step route for ·O<sub>2</sub><sup>-</sup> generation. Previous studies showed that intrinsic defects and vacancies can lead to the formation of localized acceptor states (V<sub>D</sub>) [64]. These

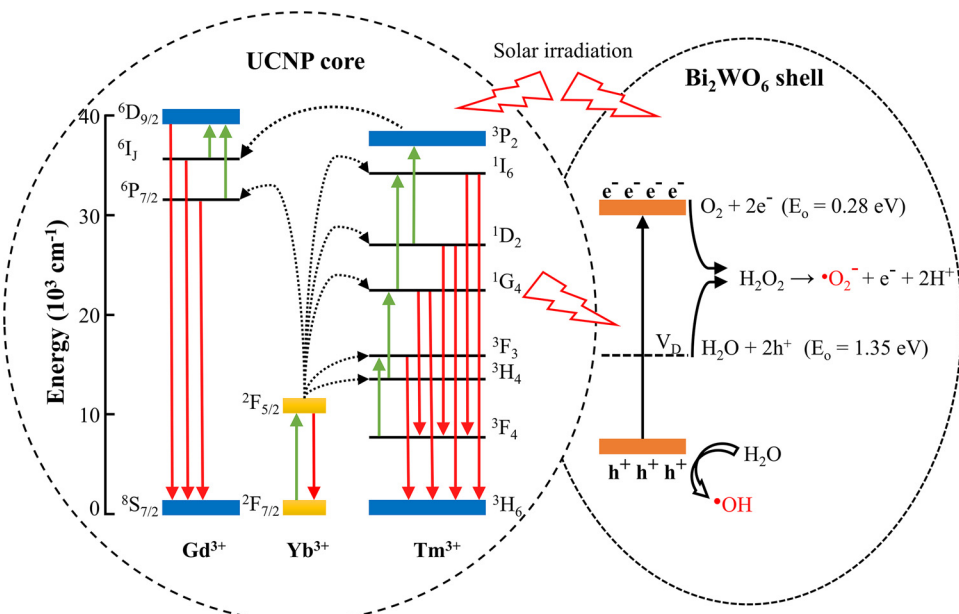


Fig. 8. Schematic illustration of energy levels and transitions in the UCNP core and transfer of energy from UCNP to Bi<sub>2</sub>WO<sub>6</sub> to produce reactive oxygen species.

Table 2

Performance evaluation of photocatalyst systems for organic contaminant degradation.

No.	Photocatalyst	Contaminant	Light source	Time (min)	Energy consumption (Wh/μmole)	Catalyst dosage (g/L)	Quantum yield (molecules/photon)	Figure of merit	Reference
1.	g-C <sub>3</sub> N <sub>4</sub> /CdS/RGO	Rhodamine B	UV	20	47.9	0.4	1.98 × 10 <sup>-6</sup>	100.0	[68]
2.	g-C <sub>3</sub> N <sub>4</sub> /RGO	Rhodamine B	UV	30	71.9	0.4	1.32 × 10 <sup>-6</sup>	44.4	[68]
3.	g-C <sub>3</sub> N <sub>4</sub> /CdS/RGO	Rhodamine B	Vis	60	47.9	0.4	1.26 × 10 <sup>-6</sup>	33.3	[68]
4.	BN/CdS	Rhodamine B	Vis	90	14.1	0.6	5.64 × 10 <sup>-6</sup>	30.7	[69]
5.	g-C <sub>3</sub> N <sub>4</sub> /BiOI	Rhodamine B	Vis	50	121.0	0.1	5.00 × 10 <sup>-7</sup>	25.3	[70]
6.	g-C <sub>3</sub> N <sub>4</sub> /CdS	Rhodamine B	UV	40	95.8	0.4	9.92 × 10 <sup>-7</sup>	25.0	[68]
7.	RGO/CdS	Rhodamine B	UV	40	95.8	0.4	9.92 × 10 <sup>-7</sup>	25.0	[68]
8.	Ag <sub>3</sub> PO <sub>4</sub> /CeO <sub>2</sub>	Rhodamine B	Vis	60	65.3	0.4	9.25 × 10 <sup>-7</sup>	24.5	[71]
9.	BiVO <sub>4</sub> /Ag <sub>3</sub> VO <sub>4</sub>	Rhodamine B	Vis	20	41.6	1.0	1.45 × 10 <sup>-6</sup>	18.4	[72]
10.	RGO/CdS	Rhodamine B	Vis	150	119.8	0.4	5.05 × 10 <sup>-7</sup>	5.3	[68]
11.	TiO <sub>2</sub>	Reactive black	UV	300	9.7	2.0	9.81 × 10 <sup>-6</sup>	13.2	[73]
12.	TiO <sub>2</sub>	Patent Blue VF	UV	80	22.9	1.0	3.82 × 10 <sup>-6</sup>	20.9	[74]
13.	Bi <sub>2</sub> S <sub>3</sub> /TiO <sub>2</sub> /RGO	Methylene blue	Vis	90	39.3	0.4	1.54 × 10 <sup>-6</sup>	54.2	[75]
14.	ZnS/CdS	Methylene Blue	Vis	180	148.1	0.1	4.08 × 10 <sup>-7</sup>	34.5	[76]
15.	CdS	Methylene Blue	Vis	360	533.1	0.1	1.13 × 10 <sup>-7</sup>	4.8	[76]
16.	WO <sub>3</sub> /NiWO <sub>4</sub>	Methylene blue	UV	400	41.2	0.6	2.31 × 10 <sup>-6</sup>	5.7	[77]
17.	TiO <sub>2</sub>	Methylene Blue	Vis	360	253.9	0.1	2.38 × 10 <sup>-7</sup>	10.1	[73]
18.	BiVO <sub>4</sub> /Ag <sub>3</sub> VO <sub>4</sub>	Methyl violet	Vis	40	72.5	1.0	8.34 × 10 <sup>-7</sup>	5.3	[72]
19.	CdS	Methyl red	UV	180	35.1	1.0	2.34 × 10 <sup>-6</sup>	4.8	[78]
20.	Graphene/TiO <sub>2</sub>	Methyl Orange	UV	20	34.6	0.6	1.76 × 10 <sup>-6</sup>	28.1	[79]
21.	Cu <sub>0</sub> /BiVO <sub>4</sub>	Bisphenol A	Vis	5	794.0	0.5	1.73 × 10 <sup>-7</sup>	9.3	[80]
22.	g-C <sub>3</sub> N <sub>4</sub>	Bisphenol A	Vis	60	68.5	0.5	1.91 × 10 <sup>-6</sup>	7.5	[81]
23.	rGO/TiO <sub>2</sub>	Bisphenol A	UV	120	40.6	1.0	3.22 × 10 <sup>-6</sup>	1.6	[82]
24.	SrTiO <sub>3</sub> /Ag/AgCl	Bisphenol A	Vis	30	35.3	0.5	3.70 × 10 <sup>-6</sup>	28.9	[83]
25.	Ag/C <sub>3</sub> N <sub>4</sub>	Bisphenol A	Vis	240	291.8	0.6	4.48 × 10 <sup>-7</sup>	0.2	[84]
This study	Bisphenol A	Solar	180	4.7	0.3	3.16 × 10 <sup>-5</sup>	72.2		

acceptor states are higher than the original valence band minimum and can provide additional sites for photochemical reactions. As shown in Fig. 8, H<sub>2</sub>O and O<sub>2</sub> were first converted to H<sub>2</sub>O<sub>2</sub> at V<sub>D</sub> and CB, respectively. In the second step, H<sub>2</sub>O<sub>2</sub> disintegrated under irradiation, producing the O<sub>2</sub><sup>·</sup> radicals that were detected during the scavenging experiments [65]. The UV-vis-NIR response of the composite that generated OH and O<sub>2</sub><sup>·</sup> radicals resulted in high BPA degradation.

### 3.8. Performance evaluation

Important photocatalytic characteristics, such as the type of contaminant, light source, product yield, contaminant load, mass of catalyst, energy consumed, and final product, can vary from one study to

another. Previously, quantum yield (QY) was used to evaluate the performance of photocatalyst systems [66,67]. However, QY alone is insufficient, therefore, we calculated a figure of merit (FOM) based on important operational parameters, as follows [38]:

$$FOM = \frac{\text{Product obtained (L)}}{\text{Catalyst dosage (g/L)} \times \text{Time (h)} \times \text{Energy consumption (Wh/μmole)}} \quad (5)$$

For simplification, the highest FOM obtained was set to 100. Then, all the other FOMs were calculated proportionally. Modified FOMs with corresponding system QYs are listed in Table 2. The FOMs show both a direct and an inverse relationship with the QYs of photocatalysts. For

instance, the QY of ZnS/CdS is 7 times smaller than that of the SrTiO<sub>3</sub>/Ag/AgCl composite, but the FOM of the former is larger. On the contrary, the FOM/QY ratios of g-C<sub>3</sub>N<sub>4</sub>/RGO and ZnS/CdS show a direct relationship. The two different trends accentuate the importance of the FOM to categorize system performance in a broad context. The highest FOM (100) was observed for the g-C<sub>3</sub>N<sub>4</sub>/CdS/RGO composite under UV, which dropped to 33 under visible light. The FOM of the UCNP@Bi<sub>2</sub>WO<sub>6</sub> composite (72) is smaller than that of the g-C<sub>3</sub>N<sub>4</sub>/CdS/RGO composite, but the irradiation source for the latter was UV, which forms only 5–6% of the solar spectrum. Comparing the performance of the g-C<sub>3</sub>N<sub>4</sub>/CdS/RGO composite in UV-vis light with that of the UCNP@Bi<sub>2</sub>WO<sub>6</sub> under solar radiation indicates that the novel nanocomposite presented in this research can offer great utility for solar-driven photoreactions.

#### 4. Conclusion

We synthesized a novel composite of UCNP@Bi<sub>2</sub>WO<sub>6</sub> and presented a new synthesis method to overcome the disintegration of UCNP during photocatalyst shell formation. Neither the UCNPs nor the Bi<sub>2</sub>WO<sub>6</sub> exhibited catalytic activity in NIR, but the UCNP@Bi<sub>2</sub>WO<sub>6</sub> degraded BPA in low-energy NIR radiation. FRET was used for energy transfer because of the absorption/emission spectral overlapping and close interfacial core/shell contact. ·OH and ·O<sub>2</sub><sup>−</sup> radicals were generated in the reaction mixture under NIR, which accounted for the increase in the composite's photoactivity under solar radiation. The high photocurrent response suggests that UCNP@Bi<sub>2</sub>WO<sub>6</sub> could be used for photoelectrochemical water splitting as well. Our results provide a framework for future studies of NIR-based photocatalysts for complete exploitation of solar energy.

#### Conflicts of interest

There are no conflicts to declare.

#### Acknowledgements

This study was supported by the Basic Science Research Program through the National Research Foundation of Korea (NRF) funded by the Ministry of Science, ICT, & Future Planning (No. 2018R1A2A1A05023555).

#### Appendix A. Supplementary data

Supplementary material related to this article can be found, in the online version, at doi:<https://doi.org/10.1016/j.apcatb.2018.10.074>.

#### References

- [1] G. Li, D. Zhang, J.C. Yu, M.K.H. Leung, *Environ. Sci. Technol.* 44 (2010) 4276–4281.
- [2] O. Ola, M.M. Maroto-Valer, *J. Photochem. Photobiol. C Photochem. Rev.* 24 (2015) 16–42.
- [3] M. Mishra, D.-M. Chun, *Appl. Catal. A Gen.* 498 (2015) 126–141.
- [4] Z. Frontistis, M. Antonopoulou, A. Petala, D. Venieri, I. Konstantinou, D.I. Kondarides, D. Mantzavinos, *J. Hazard. Mater.* 323 (2017) 478–488.
- [5] Y. Shiraishi, S. Kanazawa, Y. Sugano, D. Tsukamoto, H. Sakamoto, S. Ichikawa, T. Hirai, *ACS Catal.* 4 (2014) 774–780.
- [6] K.M. Lee, C.W. Lai, K.S. Ngai, J.C. Juan, *Water Res.* 88 (2016) 428–448.
- [7] V. Muhr, S. Wilhelm, T. Hirsch, O.S. Wolfbeis, *Accounts Chem. Res.* 47 (2014) 3481–3493.
- [8] Z. Xu, M. Quintanilla, F. Vetrone, A.O. Govorov, M. Chaker, D. Ma, *Adv. Funct. Mater.* 25 (2015) 2950–2960.
- [9] Y. Tang, W. Di, X. Zhai, R. Yang, W. Qin, *ACS Catal.* 3 (2013) 405–412.
- [10] W. Qin, D. Zhang, D. Zhao, L. Wang, K. Zheng, *Chem. Commun. (Camb.)* 46 (2010) 2304–2306.
- [11] F. Zhang, W.-N. Wang, H.-P. Cong, L.-B. Luo, Z.-B. Zha, H.-S. Qian, *Part. Part. Syst. Charact.* 34 (2017) 1600222.
- [12] W.-N. Wang, C.-X. Huang, C.-Y. Zhang, M.-L. Zhao, J. Zhang, H.-J. Chen, Z.-B. Zha, T. Zhao, H.-S. Qian, *Appl. Catal. B: Environ.* 224 (2018) 854–862.
- [13] M. Zhao, W. Wang, C. Huang, W. Dong, Y. Wang, S. Cheng, H. Wang, H. Qian, *Chinese. J. Catal.* 39 (2018) 1240–1248.
- [14] B. Zheng, Q. Guo, D. Wang, H. Zhang, Y. Zhu, S. Zhou, *J. Am. Ceram. Soc.* 98 (2015) 136–140.
- [15] C. Li, F. Wang, J. Zhu, C.Y. Jimmy, *Appl. Catal. B: Environ.* 100 (2010) 433–439.
- [16] M. Tou, Z. Luo, S. Bai, F. Liu, Q. Chai, S. Li, Z. Li, *Mater. Sci. Eng. C* 70 (2017) 1141–1148.
- [17] L. Sun, R. Wei, J. Feng, H. Zhang, *Coord. Chem. Rev.* 364 (2018) 10–32.
- [18] L. Wang, X. Li, Z. Li, W. Chu, R. Li, K. Lin, H. Qian, Y. Wang, C. Wu, J. Li, *Adv. Mater.* 27 (2015) 5528–5533.
- [19] X. Chen, L. Jin, W. Kong, T. Sun, W. Zhang, X. Liu, J. Fan, S.F. Yu, F. Wang, *Nat. Commun.* 7 (2016) 10304.
- [20] Y.-L. Wang, N.M. Estakhri, A. Johnson, H.-Y. Li, L.-X. Xu, Z. Zhang, A. Alù, Q.-Q. Wang, C.-K.K. Shih, *Sci. Rep.-Uk.* 5 (2015) 10196.
- [21] M. Wang, Y. Zhu, C. Mao, *Langmuir* 31 (2015) 7084–7090.
- [22] H. Dong, L.D. Sun, C.H. Yan, *Chem. Soc. Rev.* 44 (2015) 1608–1634.
- [23] D.T. Klier, M.U. Kumke, *J. Phys. Chem. C* 119 (2015) 3363–3373.
- [24] Y. Huang, S. Kang, Y. Yang, H. Qin, Z. Ni, S. Yang, X. Li, *Appl. Catal. B: Environ.* 196 (2016) 89–99.
- [25] Y. Zhou, X. Meng, L. Tong, X. Zeng, X. Chen, *Energies* 9 (2016) 764.
- [26] X. Lin, Z. Liu, X. Guo, C. Liu, H. Zhai, Q. Wang, L. Chang, *Mater. Sci. Eng. B* 188 (2014) 35–42.
- [27] S. Sun, W. Wang, J. Xu, L. Wang, Z. Zhang, *Appl. Catal. B: Environ.* 106 (2011) 559–564.
- [28] R. Cao, H. Huang, N. Tian, Y. Zhang, Y. Guo, T. Zhang, *Mater. Charact.* 101 (2015) 166–172.
- [29] M.B. Grawande, A. Goswami, T. Asefa, H. Guo, A.V. Biradar, D.-L. Peng, R. Zboril, R.S. Varma, *Chem. Soc. Rev.* 44 (2015) 7540–7590.
- [30] D. Chen, K. Kannan, H. Tan, Z. Zheng, Y.-L. Feng, Y. Wu, M. Widelka, *Environ. Sci. Technol.* 50 (2016) 5438–5453.
- [31] P.V.L. Reddy, K.-H. Kim, B. Kavitha, V. Kumar, N. Raza, S. Kalagara, *J. Environ. Manage.* 213 (2018) 189–205.
- [32] J. Di, J. Xia, Y. Ge, H. Li, H. Ji, H. Xu, Q. Zhang, H. Li, M. Li, *Appl. Catal. B: Environ.* 168–169 (2015) 51–61.
- [33] J. Yu, J. Xiong, B. Cheng, Y. Yu, J. Wang, *J. Solid State Chem.* 178 (2005) 1968–1972.
- [34] R. Zhou, X. Li, *Opt. Mater. Express* 6 (2016) 1313–1320.
- [35] M.A. Calil Júnior, Á.A.C. Melo, E.M. Rodrigues, F.A. Sigoli, M.O. Rodrigues, *J. Brazil. Chem. Soc.* 28 (2017) 1816–1821.
- [36] J. Lan, F. Wen, F. Fu, X. Zhang, S. Cai, Z. Liu, D. Wu, C. Li, J. Chen, C. Wang, *RSC Adv.* 5 (2015) 18008–18012.
- [37] M. Li, L. Zhang, X. Fan, Y. Zhou, M. Wu, J. Shi, *J. Mater. Chem. A Mater. Energy Sustain.* 3 (2015) 5189–5196.
- [38] H. Anwer, J.-W. Park, *J. Hazard. Mater.* (2018).
- [39] N.M. El-Ashgar, I.M. El-Nahhal, M.M. Chehimi, F. Babonneau, J. Livage, *Int. J. Environ. An.* (2009) 1057–1069 Ch. 89.
- [40] M. Chirita, A. Ieta, *Cryst. Growth Des.* 12 (2012) 883–886.
- [41] G. Zhao, S. Liu, Q. Lu, F. Xu, H. Sun, *J. Alloys. Compd.* 578 (2013) 12–16.
- [42] B. Zhang, X. Ye, C. Wang, Y. Xie, *J. Mater. Chem.* 17 (2007) 2706–2712.
- [43] X.-Y. Yu, B.-X. Lei, D.-B. Kuang, C.-Y. Su, *Chem. Sci.* 2 (2011) 1396–1400.
- [44] X. Hu, D. Pan, H. Han, M. Lin, Y. Zhu, C. Wang, *Mater. Lett.* 190 (2017) 83–85.
- [45] L. Xiang, L. Chen, C.-H. Mo, L.-M. Zheng, Z.-X. Yu, Y.-W. Li, Q.-Y. Cai, H. Li, W.-D. Yang, D.-M. Zhou, M.-H. Wong, *J. Mater. Sci.* 53 (2018) 7657–7671.
- [46] Z. Shiyu, Z. Qiyuan, Z. Deqiang, Z. Wenjuan, F. Zihong, S. Yaofang, X. Xuan, *Appl. Organomet. Chem.* 32 (2018) e4230.
- [47] F. Wu, H. Su, X. Zhu, K. Wang, Z. Zhang, W.-K. Wong, *J. Mater. Chem. B Mater. Biol. Med.* 4 (2016) 6366–6372.
- [48] W.C. Lang, B.D. Padalia, L.M. Watson, D.J. Fabian, P.R. Norris, *Faraday Discuss.* *Chem. Soc.* 60 (1975) 37–43.
- [49] Q. Yin, X. Jin, G. Yang, C. Jiang, Z. Song, G. Sun, *RSC Adv.* 4 (2014) 53561–53569.
- [50] J. Tauc, *Mater. Res. Bull.* 3 (1968) 37–46.
- [51] R. López, R. Gómez, J. Solgel Sci. Technol. 61 (2012) 1–7.
- [52] A.J. Deotale, R.V. Nandedkar, *Mater. Today-Proc.* 3 (2016) 2069–2076.
- [53] M. Quintanilla, I.X. Cantarelli, M. Pedroni, A. Speghini, F. Vetrone, *J. Mater. Chem. C Mater. Opt. Electron. Devices* 3 (2015) 3108–3113.
- [54] M. Li, X. Liu, L. Liu, B. Ma, B. Li, X. Zhao, W. Tong, X. Wang, *Inorg. Chem. Front.* 3 (2016) 1082–1090.
- [55] H. Qiu, C. Yang, W. Shao, J. Damasco, X. Wang, H. Ågren, P. Prasad, G. Chen, *Nanomater.* 4 (2014) 55.
- [56] T. Jiang, Y. Liu, S. Liu, N. Liu, W. Qin, *J. Colloid Interf. Sci.* 377 (2012) 81–87.
- [57] K. Zhang, S. Zhou, Y. Zhuang, R. Yang, J. Qiu, *Opt. Express* 20 (2012) 8675–8680.
- [58] L. Mattsson, K.D. Wegner, N. Hildebrandt, T. Soukka, *RSC Adv.* 5 (2015) 13270–13277.
- [59] X. Gao, X. Liu, Z. Zhu, X. Wang, Z. Xie, *Sci. Rep.-Uk.* 6 (2016) 30543.
- [60] G. Cheng, J. Wu, F. Xiao, H. Yu, Z. Lu, X. Yu, R. Chen, *Mater. Lett.* 63 (2009) 2239–2242.
- [61] F.I. López-Salinas, G.A. Martínez-Castañón, J.R. Martínez-Mendoza, F. Ruiz, *Mater. Lett.* 64 (2010) 1555–1558.
- [62] X. Chen, D. Peng, Q. Ju, F. Wang, *Chem. Soc. Rev.* 44 (2015) 1318–1330.
- [63] M. Butler, D. Ginley, *J. Electrochem. Soc.* 125 (1978) 228–232.
- [64] Y.P. Xie, Z.B. Yu, G. Liu, X.L. Ma, H.-M. Cheng, *Synth. Lect. Energy Environ. Technol. Sci. Soc.* 7 (2014) 1895–1901.
- [65] R.J. Mailloux, *Redox Biol.* 4 (2015) 381–398.
- [66] H. Kisch, D. Bahnamann, *J. Phy. Chem. Lett.* 6 (2015) 1907–1910.
- [67] J. Krýsa, M. Baudys, A. Mills, *Catal. Today* 240 (2015) 132–137.
- [68] R.C. Pawar, V. Khare, C.S. Lee, *Dalton Trans.* 43 (2014) 12514–12527.
- [69] X. Li, F. Qi, Y. Xue, C. Yu, H. Jia, Y. Bai, S. Wang, Z. Liu, J. Zhang, C. Tang, *RSC Adv.*

5 (2016) 99165–99171.

[70] J. Di, J. Xia, S. Yin, H. Xu, L. Xu, Y. Xu, M. He, H. Li, *J. Mater. Chem. A Mater. Energy Sustain.* 2 (2014) 5340–5351.

[71] W. Zhang, C. Hu, W. Zhai, Z. Wang, Y. Sun, F. Chi, S. Ran, X. Liu, Y. Lv, *Mater. Res.* 8 (2016) 673–679.

[72] M. Yan, Y. Wu, Y. Yan, X. Yan, F. Zhu, Y. Hua, W. Shi, *ACS Sustain. Chem. Eng.* 4 (2016) 757–766.

[73] A. Aguedach, S. Brosillon, J. Morvan, E.K. Lhadi, *Appl. Catal. B: Environ.* 57 (2005) 55–62.

[74] M. Qamar, M. Saquib, M. Muneer, *Dye. Pigment.* 65 (2005) 1–9.

[75] Y. Liu, Y. Shi, X. Liu, H. Li, *Appl. Surf. Sci.* 396 (2017) 58–66.

[76] N. Soltani, E. Saion, W.M.M. Yunus, M. Erfani, M. Navasery, G. Bahmanrokh, K. Rezaee, *Appl. Surf. Sci.* 290 (2014) 440–447.

[77] M.M. Mohamed, S.A. Ahmed, K.S. Khairou, *Appl. Catal. B: Environ.* 150–151 (2014) 63–73.

[78] E. Repo, S. Rengaraj, S. Pulkka, E. Castangnoli, S. Suihkonen, M. Sopanen, M. Sillanpää, *Sep. Purif. Technol.* 120 (2013) 206–214.

[79] B. Tang, H. Chen, Y. He, Z. Wang, J. Zhang, J. Wang, *Compos. Sci. Technol.* 10 (2017) 54–64.

[80] Y. Kanigaridou, A. Petala, Z. Frontistis, M. Antonopoulou, M. Solakidou, I. Konstantinou, Y. Deligiannakis, D. Mantzavinos, D.I. Kondarides, *Chem. Eng. J.* 318 (2017) 39–49.

[81] B. Liu, M. Qiao, Y. Wang, L. Wang, Y. Gong, T. Guo, X. Zhao, *Chemosphere.* 189 (2017) 115–122.

[82] L. Luo, Y. Yang, A. Zhang, M. Wang, Y. Liu, L. Bian, F. Jiang, X. Pan, *Appl. Surf. Sci.* 353 (2015) 469–479.

[83] S.-F. Yang, C.-G. Niu, D.-W. Huang, H. Zhang, C. Liang, G.-M. Zeng, *Environ. Sci. Nano* 4 (2017) 585–595.

[84] W.-D. Oh, L.-W. Lok, A. Veksha, A. Giannis, T.-T. Lim, *Chem. Eng. J.* 333 (2018) 739–749.